



LAWRENCE
LIVERMORE
NATIONAL
LABORATORY

Research and Development of Non-Spectroscopic MEMS-Based Sensor Arrays for Targeted Gas Detection

A. Loui, S. K. McCall, J. M. Zumstein

December 5, 2012

Disclaimer

This document was prepared as an account of work sponsored by an agency of the United States government. Neither the United States government nor Lawrence Livermore National Security, LLC, nor any of their employees makes any warranty, expressed or implied, or assumes any legal liability or responsibility for the accuracy, completeness, or usefulness of any information, apparatus, product, or process disclosed, or represents that its use would not infringe privately owned rights. Reference herein to any specific commercial product, process, or service by trade name, trademark, manufacturer, or otherwise does not necessarily constitute or imply its endorsement, recommendation, or favoring by the United States government or Lawrence Livermore National Security, LLC. The views and opinions of authors expressed herein do not necessarily state or reflect those of the United States government or Lawrence Livermore National Security, LLC, and shall not be used for advertising or product endorsement purposes.

This work performed under the auspices of the U.S. Department of Energy by Lawrence Livermore National Laboratory under Contract DE-AC52-07NA27344.

32200 (DSW-MTP)
FY12 Report: Noble Gas Detection (540809)

*Research and Development of Non-Spectroscopic MEMS-Based Sensor Arrays
for Targeted Gas Detection*

A. Loui, S.K. McCall, and J.M. Zumstein

1.1 Introduction

In this report, we present our progress during Fiscal Year 2012 (FY12) in the research and development of a non-spectroscopic method for noble gas detection. During Fiscal Year 2011 (FY11), we demonstrated that coating-free damped resonance detection (cfDRD) could be used for the selective sensing of pure gases and simple (binary) admixtures.¹ Specifically, it was found that a sensor response signature comprised of both resonant peak shape change and frequency shift data exhibited increased chemical selectivity over a response signature based only on the latter contribution. The sensor response signature is presently comprised of three distinct data inputs: two channels from the cfDRD sensor component [shape change (attenuation/amplification), frequency shift], and one from a thermal conductivity detection (TCD) sensor component. A single commercial-off-the-shelf (COTS) resonator (Bruker Active Probe microcantilever) was excited into either its 1st or 4th resonant modes, where it was found that the latter was apparently insensitive to compositional changes in the surrounding gas; this difference was attributed to the ~20x difference in average flexural displacement in the former versus the latter, and the expected dominance of inertial effects in the damping phenomenon.¹

The recent study by Naeli and Brand demonstrated a method of thermal drift self-compensation for a resonating microcantilever coated with a chemically functional film;² these authors showed that thermally-induced frequency drift – represented by a temperature coefficient of frequency (TCF) – was nearly identical for several examined resonance modes, while the damping response due to analyte sorption into the functional film varied for the same modes. Thus, by driving a single resonator alternately between a pair of such resonances, the thermal drift could be effectively cancelled out by taking the differential damping response (frequency shift in this prior study). This general concept is being explored in the current project, where the resonance changes are caused by inertial damping in, rather than sorption of, the gas-phase analyte. For the COTS resonator, what remains to be demonstrated is that its thermal drift response is identical for the 1st and 4th resonances. An experimental apparatus for testing this concept is described, followed by a brief presentation of data. Next, we outline an algorithm for fitting a curve to sparse resonator data in the frequency domain, which may alleviate the need for the data-, processor-, and time-intensive acquisition/storage of high-frequency-resolution spectra. The Bruker Active Probe (\$75/unit per 10 count)³ is a piezoelectrically driven microcantilever designed for applications related to atomic force microscopy (AFM); while commercially available for a number of years, the specialized device has a limited market demand. Therefore, we have developed a new test platform for cfDRD based on a mass-produced, high-precision, and low-cost (e.g., \$0.66/unit per 100 count for ECS-31X)⁴ quartz crystal tuning fork widely used as a stable frequency source in timing devices (for example). The breadboard-level

prototype integrates the phase-locked loop and AC drive signal functions, which are implemented with digital and analog integrated circuits; this advancement replaces the benchtop-scale test instrumentation (lock-in amplifier; function generator and oscilloscope) used during FY11, and defines the hardware architecture for a miniaturized, self-contained, sensor array system. We conclude the report with a brief discussion of the future developmental path for the TCD sub-sensor.

1.2 Thermal Drift Testing Apparatus

The thermal drift testing apparatus is currently comprised of several components: 1) sensor transducers; 2) gas cell; 3) mass flow controllers; 4) hotplate and; 5) temperature controller. Detailed descriptions of this apparatus can be found in Section 1.3.3 and Appendix C of our previous report.¹ The dual-chambered gas cell was designed to house the cfDRD and TCD sensor transducers in leak-free gas volumes (for reference and test gases) while providing a high thermal conductivity path to an external heating element (hotplate). The cells were designed to hold gases either dynamically or statically; at present, sensor testing is performed under dynamic conditions at ambient pressure, with flow regulated by digital mass flow controllers. Each chamber is thus outfitted with a gas inlet and outlet, with static operation simply enabled by fitting one port with a blank and using the other for gas backfilling and evacuation. Fabrication of the gas cell occurred during the first quarter (Q1) of FY12.

During assembly, the vacuum-compatible epoxy resin (Loctite 1C Hysol) originally intended as the joint sealant proved too viscous for highly-localized application – for example, at the perimeters of the 0.064” diameter spring loaded pins used as electrical contacts for the TCD transducer (Ref. 1, Appendix C). Vacuum-compatible leak sealant (SPI Supplies Vacseal II), which is an air-curable liquid polymer (dimethyldiphenyl siloxane), was used as a replacement; a fine bead of sealant was applied to each joint using a syringe and 18 gauge hypodermic needle, with the liquid drawing into the joint by capillary action. The electrical feedthrough pins were secured into the Delrin insulator plates – which form the floor of each cell chamber – via interference fit alone, with no strain relief for the external wiring to be soldered to the brass alloy pins. Any tension forces transmitted along the wiring will create shear stress within the joint sealant, which could lead to adhesive delamination and a loss of gas integrity in the cell chambers. The lap shear strength of the sealant is considerably less than that of the epoxy (0.15 N/mm² vs. 12.1 N/mm², respectively);^{5, 6} not surprisingly, the former is not recommended as a load-bearing adhesive (hence, the classification as a ‘sealant’). To prevent this possibility, an aluminum plate was designed which attaches to the bottom of the gas cell, providing a rigid location for a wiring terminal block as well as a high thermal conductivity interface between the gas cell and underlying hotplate. The assembled gas cell, in the dynamic gas flow configuration, is shown in Fig. 1. A detailed wiring diagram is also provided for reference in Appendix A.

1.2.1 Thermal Drift Data

As discussed in Section 1.3.1 in our previous report,¹ the excitation of the COTS resonator at its fundamental (~57.4 kHz) and overtone (>100 kHz) modes required the use of two sets of benchtop instrumentation: 1) Stanford Research Systems SR830 lock-in amplifier (0-100 kHz); 2) Agilent 33120A function generator and Tektronix TDS 3012B oscilloscope (up to 15 MHz). Both of these test setups suffer from noise which makes it difficult to assess the relatively small frequency shifts for a particular resonance peak as a function of temperature. As an expe-

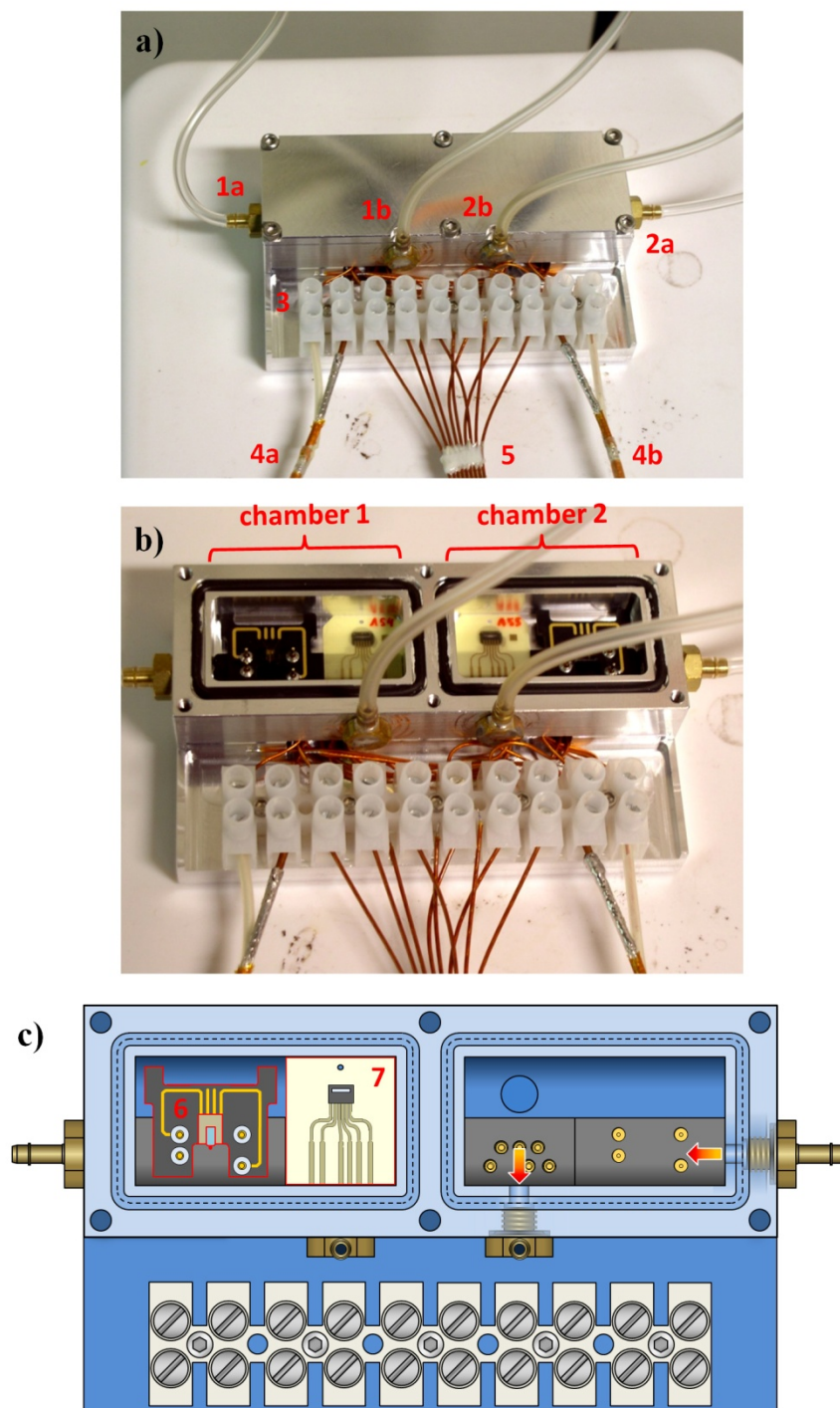


Figure 1. Dual-chambered gas cell for thermal drift testing. a) Photograph of cell, showing the gas inlet (1a and 2a) and outlet (1b and 2b) connections for cell chambers 1 and 2, respectively. The external wiring from the electronics (not shown) to the 10-wire terminal block (3) includes cfDRD (4a and 4b) and TCD (5) connections. b) Photograph of cell, with gas-tight lid removed to reveal the chambers and enclosed sensor transducers. c) Schematic representation of cell, showing the location of the cfDRD [Bruker Active Probe (6)] and TCD [Canton CantiChip4 (7)] transducers in the left cell chamber. The direction of dynamic gas flow is shown in the empty right cell chamber.

dient, a simple moving average filter with a symmetric boxcar function was applied to each data point of the frequency spectra. A plot of the fundamental resonance in N_2 at 21°C and 83°C is shown in Fig. 2, where a boxcar width of 7 data points is applied to data of 1 Hz resolution; this data represents an average of three separate measurements, with an average phase error of -0.4% demonstrating the reproducibility in resonant response. An estimated frequency reduction of 10 Hz for the temperature change $+62^\circ\text{C}$ ($21^\circ\text{C} \rightarrow 83^\circ\text{C}$) yields a TCF of -2.8 parts-per-million per Kelvin (ppm/K). Measurements under the same conditions in He gave a TCF value of -2.5 ppm/K. In the current setup, noise artifacts near the resonance peak can distort the assessment of corresponding frequency on the order of 10 Hz, which leads to a factor of two uncertainty in the TCF; we therefore regard the numerical coincidence of these two measurements with caution. We note that the true temperature of the transducer was estimated by inserting a thermocouple probe into the body of the high thermal conductivity gas cell, since direct attachment to the microscopic and fragile resonator chip was not technically feasible; as will be discussed below, theoretical calculations show that the observed frequency reduction is actually consistent with a much smaller temperature change (and hence, larger TCF) than indicated by the indirect measurements. Unlike the TCD sub-sensor, which relies on differences in the heat dissipation efficiency of gases, the cfDRD sub-sensor should experience negligible self-heating due to its small power dissipation (estimated at 90 nW in the test circuit).

Guided by the findings of Naeli and Brand, we next sought to demonstrate a high similarity in TCF between the gas-insensitive overtone at ~ 399 kHz and the fundamental mode. To achieve the -2.5 ppm/K value determined for the fundamental resonance in N_2 , under the presumption of accurate transducer temperature measurement, an equivalent frequency shift of -62 Hz should be measured. A plot of the 4th resonance in N_2 at 21°C and 83°C is shown in Fig. 3, where a boxcar width of 25 data points is applied to data of 5 Hz resolution; this data also represents an average of three separate measurements, with an average phase error of 0.4% . Noise artifacts make identification of the peak frequency more difficult (Fig. 3b); however, a frequency decrement of -90 Hz is estimated for the temperature change $+62^\circ\text{C}$ ($21^\circ\text{C} \rightarrow 83^\circ\text{C}$),

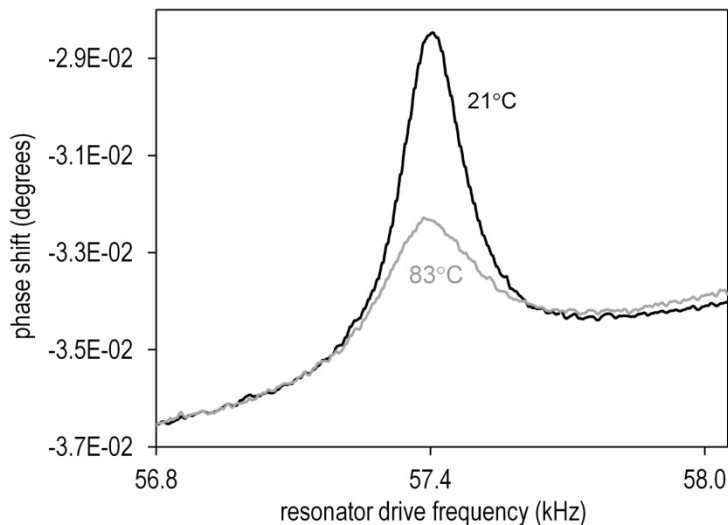


Figure 2. Frequency spectra for the fundamental resonance mode of a Bruker Active Probe cantilever in N_2 . The resonant response at 21°C and 83°C was achieved using the gas cell shown in Fig. 1.

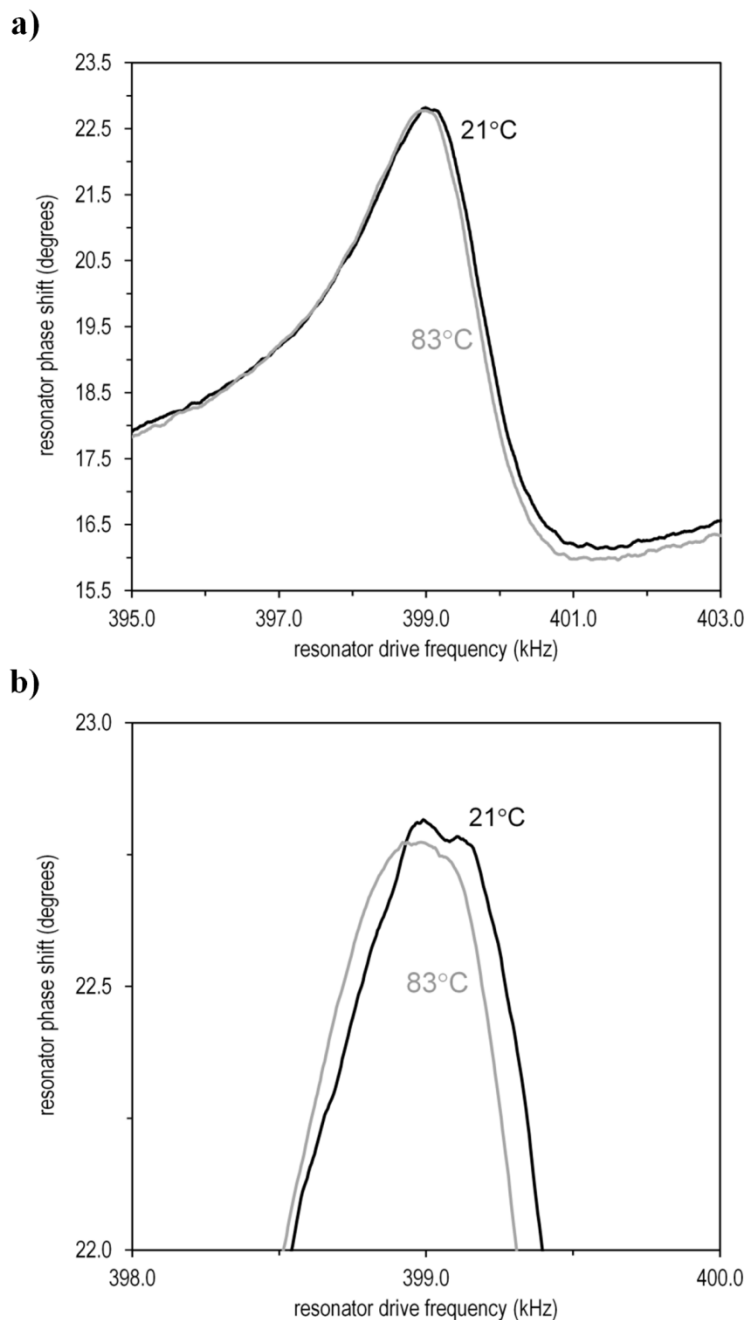


Figure 3. Frequency spectra for the overtone resonance mode of a Bruker Active Probe cantilever at 399 kHz in N_2 . The resonant response at 21°C and 83°C was achieved using the gas cell shown in Fig. 1.

yielding a TCF of -3.6 ppm/K. Given the phase noise inherent in both test setups, these preliminary measurements appear to indicate that the thermal drift in resonance frequency for these two modes is very similar. Our findings can be generally compared to the prior result of Naeli and Brand, who reported a common TCF value of -19.5 ppm/K for their electromagnetically-actuated, rectangular microcantilevers.²

The election to perform thermal drift testing in different gases was originally motivated by the chief goal of this project: to develop a leak detector for noble and other gases of interest. Under most practical applications, this mandate requires operation under potentially dynamic temperature conditions. Since the TCF is an intrinsic property of the resonator, its correct assessment relies on subjecting the device to an accurately measured temperature change, and noting the resultant changes in resonance frequency *in the absence of any other effect which may also cause the resonance condition to change*. Aside from the technical difficulty of direct temperature measurement, as noted above, it is obvious in retrospect that the assessment of TCF should have been performed under evacuated conditions to eliminate the possibility of thermally-induced changes in gaseous damping. These considerations raise a very crucial point in the present case of cfDRD: **the thermal drift that we seek to eliminate arises exclusively from the intrinsic characteristics of the resonator**. Generally, the temperature of the resonator and its surrounding gas medium will both change, such that the damped resonance condition will be altered both by the thermal drift in the resonator response (an ‘internal’ effect represented by the TCF) and actual temperature-related changes in the gas properties themselves (an ‘extrinsic’ effect, independent of the resonator). The cfDRD method relies on the detection of changes in the density and viscosity of the gaseous environment, whether those alterations are created by changes in the gas composition – such as those which occur during a leak event – or are the result of changes in temperature. The simultaneous contribution of these two effects adds further complexity to the cfDRD data interpretation. Since a viable sensor must be able to identify leaking gases regardless of the prevailing temperature condition, it becomes clear that the gas temperature should also be incorporated into the analyte data signature.

Thus, in exploring the viability of thermal drift compensation in the cfDRD method, we must take great care to deconvolve – either through direct identification or by deduction – the ‘internal’ and ‘external’ contributions to changes in resonance under dynamic temperature conditions. The former (‘internal’) constitutes thermal drift which, if shown to be substantially identical between sensing and reference channels, may be simply nullified as in the case reported by Naeli and Brand. The latter (‘external’) represents ‘real’ data conveying information about the identity of the gas. What kind of thermally-induced changes have been observed? Both the prior study by Naeli and Brand, and the data we present in Figs. 2 and 3, reveal shifts in the peak resonance frequency with changes in temperature. What is also obvious from our data is a peak shape change, similar to what occurs for gas composition changes,¹ but definitely the result of temperature effects in the present case where the gas identity remains fixed. A significant *reduction* of amplitude/quality factor (Q) was observed for the fundamental resonance in N_2 for the temperature change $+62^\circ\text{C}$ ($21^\circ\text{C} \rightarrow 83^\circ\text{C}$), while a similar decrement could not be discerned for the overtone within the uncertainty imposed by the noise. This trend contradicts that reported by Naeli and Brand, who found *increases* in Q -factor in air subjected to the temperature change $+60^\circ\text{C}$ ($10^\circ\text{C} \rightarrow 70^\circ\text{C}$);² they also determined that the apparent temperature-induced increase became *larger* with each successively higher resonance mode (fundamental: $+0.08\%$; second overtone: $+5.6\%$; third overtone: $+9.1\%$).

Since these authors did not present a theoretical justification for their reported trends, we performed micromechanical calculations to help: 1) ascertain which of the Q -factor trends – decrease or increase, with increase in temperature – is expected, and; 2) determine the relationship between the resonance changes (frequency shift, Q -factor change), and the underlying internal and external causes, such that the thermal drift contributions can be identified

Table 1. Cantilever fundamental resonance Q -factor in various heating scenarios.

<i>Experimental:</i>		<i>Scenario 1:</i>	<i>Scenario 2:</i>	<i>Scenario 3:</i>	<i>Damping Regime:</i>
21°C	83°C	N ₂ - 83°C cantilever - 83°C	N ₂ - 83°C cantilever: 21°C	N ₂ - 21°C cantilever - 83°C	
602.0714	419.0905	505.2904	505.8282	601.4308	Re >> 1
		513.4503	514.5439	600.7914	Re << 1

and isolated. Analytic expressions for the resonance behavior of cantilevers exist, but only for monolithic or laminate structures of uniform thickness and rectangular planform design undergoing small amplitude flexural oscillation; these expressions may be adapted to other planforms, including the chevron shape popularly used in contact force AFM. **With the additional complication of damping, we are forced to restrict ourselves to the closed-form solution corresponding to the fundamental resonance.** The theoretical calculations are detailed in Appendix B, and results for Q -factor changes with temperature presented in Table 1. Our calculations show that Q -factor for the fundamental resonance should decrease with increasing temperature, the result of two possible factors: 1) small decreases/increases in gaseous mass density (ρ)/viscosity (η), respectively and; 2) small reductions in the spring constant, due to a modest softening of the Young's modulus of the cantilever material (primarily silicon). Other potential damping effects, including mechanical dissipation into the support substrate, acoustic radiation into the gas, and thermoelastic heating loss within the cantilever, should all be relatively negligible (Appendix B).

Although we have previously modeled the gaseous damping of a cantilever resonator,⁷ we did not examine the relative contributions of ρ and η changes to alterations in the resonance condition; the primary reason was that we adopted the theoretical development of Blom and co-workers, where the deconvolution of ρ and η effects is non-trivial.⁸ In a similar report by Tétin and co-workers, contemporary to our previous work, changes in the resonance condition were elegantly expressed in terms of separate ρ - and η -dependent terms;⁹ these authors then found that the resonance condition of rectangular cantilevers undergoing small amplitude flexural oscillations depended primarily on the former. These authors have notionally categorized both effects as ‘viscous’ in nature, to distinguish them from mechanical damping effects intrinsic to the cantilever and its support. In the previous/present reports, we instead assigned/assign the respective terms ‘inertial’ and ‘viscous’ to clearly identify these distinct, gas-related damping dependences. Based upon the study of Tétin and co-workers, we have been operating under the assumption that inertial forces dominate the damping behavior. However, the present analysis has caused us to reconsider this result taken at face value. The Reynolds number (Re) for the relative motion of the oscillator in a gas, as the ratio of the inertial and viscous forces, provides a convenient figure of merit for determining the operational damping regime. The average oscillation speed v can be estimated for the COTS resonator. Sanz and co-workers measured the average flexural displacement for the fundamental resonance of a Bruker Active Probe at 10.5 nm for an applied bias of $0.5 V_{\text{rms}}$ using laser vibrometry;¹⁰ with a resonance frequency value of ~ 57.4 kHz, a value $v = 4(10.5 \text{ nm})(57.4 \text{ kHz}) = 2.4 \text{ mm/s}$ is obtained over one cycle of oscillation. Variations in the voltage, up to the piezoelectric breakdown voltage of $6 V_{\text{rms}}$,³ might be expected to increase this value by no more than a factor of 10. The corresponding Reynolds number for oscillation in N₂ at 21°C (for example) is then:

$$Re = \frac{\rho vl}{\eta} = \frac{(1.16 \text{ kg/m}^3)(2.4 \times 10^{-3} \text{ m/s})(400 \times 10^{-6} \text{ m})}{1.76 \times 10^{-5} \text{ Pa}} = 6.3 \times 10^{-2} \quad (1)$$

where the object dimension l is taken as the average of the total cantilever length and width. Therefore, it would appear that we are operating well within the viscous regime, in contradiction to the conclusion reached by Tétin and co-workers under similar conditions. Using sets of equations valid for inertial ($Re \gg 1$) and viscous ($Re \ll 1$) damping, we find that the resulting predictions for the Q -factor are not sufficiently different in magnitude to indicate the correctness of either assumption. One consideration which is not incorporated into the equations utilized in the present work, but was accounted in the calculations of Tétin and co-workers, is the presence of a viscous fluid layer surrounding the resonator;⁹ the presence of this persistent, stagnant layer, which is on the order of 10 μm in thickness, may explain the apparent discrepancy. This gas-related phenomenon may also explain our observation of a substantially lower Q -factor decrement than the theoretical prediction (Table 1).

We consider several possible scenarios in which the two factors may contribute differently to the thermal behavior of the resonance condition – Scenario 1: heating/cooling is accomplished such that both the resonator and its gaseous environment are at the same temperature; Scenario 2: heating/cooling is applied *to the gas*, which is then circulated over the resonator; Scenario 3: heating/cooling is applied *to the resonator*, where the gas may or may not be circulated. In the second scenario, one might expect the resonator to be relatively cooler/warmer than the heated/cooled gas (respectively) due to poor gaseous thermal conductivity and its attachment to a relatively massive substrate support (i.e., heat sink) – for illustrative purposes, we interpret this as the implausible limiting case of the resonator remaining at ambient temperature. For the third scenario, we consider the limiting case where sufficient advection occurs such that the gas is maintained at the ambient temperature of the external supply reservoir, while the resonator is subjected to an elevated or depressed temperature. The predicted Q -factors for these three scenarios in a hypothetical case of heating are summarized in Table 1, and indicate that thermally-induced changes in gaseous damping dominate over the corresponding changes in modulus, at least for the modeled fundamental resonance. **In all cases, a decrease in Q -factor is predicted with an increase in temperature, in support of our experimental observations and in contradiction to the reported findings of Naeli and Brand.** Considering the two physical factors – external damping by the gas, and internal stiffness changes – it is difficult to imagine a condition where the Q -factor should increase with increasing temperature. For such an event to occur, the relative damping of the gas would have to decrease and/or the flexural stiffness would have to increase. The model employed in the present case has been previously vetted in a comprehensive comparative study,¹¹ so the prediction of increased gas damping based on the known temperature dependence of ρ and η seems to rest on sound theoretical footing. Our assumption of decreasing stiffness with increasing temperature is based on a softening of the effective cantilever modulus; however, it is possible that strain stiffening might occur due to thermal expansion mismatches between the adhered layers of a laminate cantilever, with greatest damping effect at oscillatory amplitudes near the nominal limits of a presumed linear restoring force (i.e., displacements much less than the cantilever thickness). This phenomenon seems unlikely in the case of the practically monolithic silicon cantilevers employed by Naeli and Brand, which were 11 μm in thickness with a 0.8 μm thick silicon dioxide encapsulation.² It is implausible that substantial differences in temperature existed between the gas and resonator in the prior case, given these authors' use of an environmental test chamber;² however, considering that heating is achieved via the gas rather

than through the resonator, any possible temperature difference which could occur would do so with a relatively cooler resonator (i.e., Scenario 2). Our calculations indicate that the largest decrease in Q -factor occurs in this condition, making the results of Naeli and Brand all the more perplexing. At present, the root cause of the prior observed behavior remains unknown.

The discrepancy between the predicted (e.g., 513) and measured (419) Q -factors may at least partially be attributed to an inaccurately low measurement of the resonator temperature, due to the restriction in temperature probe placement described above. For example, an increase in model temperature from 83°C to 103°C further reduces the predicted Q -factor to 480 or 490. In addition, the experimental value is itself an estimate, since the frequency response is not symmetric like a Gaussian distribution (for example); as a result, the resonance peak characteristics of amplitude A and full width at half maximum $FWHM$ are difficult to define precisely. Substantial decrement in the fundamental resonance Q -factor is predicted only in cases where gas heating occurs. In the present experiments, a gas flow rate of 30 standard cubic centimeters per minute (sccm) through a cell chamber volume of 3.4 cm³ defines a complete gas volume turnover time of $\Delta t = 6.8$ seconds.¹ Based on the third scenario described above – advection of an ambient temperature gas – one might expect the maintenance of a relatively cool gas volume around the heated resonator and within the cell. To determine whether the gas, during its brief transit time through the cell, can be significantly heated by thermal radiation emitted from the cell interior, we estimate the net power transfer P_{net} using the Stefan-Boltzmann law and the definition of heat capacity:

$$P_{net} = \frac{Q}{\Delta t} = \frac{m_{gas}C_{gas}\Delta T}{\Delta t} = A_s\sigma(\epsilon_{cell}T_{cell}^4 - \epsilon_{gas}T_{gas}^4) \quad (2)$$

where m_{gas} is the mass (in kg) of 3.4 cm³ of gas at ambient pressure and temperature $T_{gas} = 21^\circ\text{C}$, A_s is the total gas-exposed surface area within a test cell chamber, and σ is the Stefan-Boltzmann constant ($5.6704 \times 10^{-8} \text{ W/m}^2\text{K}^4$).¹² The gas specific heat capacity C_{gas} at temperature T_{gas} can be calculated from the empirical Shomate equation, with parameters referenced from the NIST Chemistry WebBook.¹³ The emissivity ϵ_{cell} of the polished aluminum cell is estimated at a few percent of blackbody emission (e.g., 0.03-0.06),¹⁴ while the emissivity ϵ_{gas} of the gas is estimated at ~0.04 from data reported by Leckner for CO₂ at a partial pressure-path length value of 0.8 bar-cm (i.e., 1.0 bar total pressure times a 0.8 cm path length equal to the minimum gas cell internal dimension) at the lowest available temperature (100°C).¹⁵ Substituting these values, and a cell temperature $T_{cell} = 83^\circ\text{C}$, into Eq. 2 yields a value of 47.9 mW for the net thermally radiated power from the cell into the gas. This power, over a transit time of 6.8 seconds, is sufficient to raise the temperature of N₂ ($C = 1.040 \text{ kJ/kg}\cdot\text{K}$) by approximately $\Delta T = 80^\circ\text{C}$. While Eq. 2 is more properly applied over a succession of small time steps, with diminishing radiated power into the warming gas and an accounting of volumetric gas flow (heated out, cool in), the simplified calculation above indicates that a substantial heating of the gas should occur despite the seemingly rapid advection. This provides further theoretical support for the observed decrease in fundamental resonance Q -factor with an increase in temperature.

The three heating/cooling scenarios provide insight into the relationship between the fundamental resonance changes (frequency shift, Q -factor change) and the underlying internal and external causes. In Scenario 2 (gas hot, resonator cool), a significant reduction in Q -factor is predicted, whereas in Scenario 3 (gas cool, resonator hot) the change in peak shape is negligible (Table 1). **These results imply that the thermally-induced changes to the Q -factor are primarily external to the resonator in origin, and therefore do not constitute thermal drift**

Table 2. Cantilever fundamental resonance peak change in various heating scenarios.

<i>Peak Change Quantity:</i>	<i>Experimental (21°C→83°C):</i>	<i>Scenario 1:</i>	<i>Scenario 2:</i>	<i>Scenario 3:</i>	<i>Damping Regime:</i>
		N ₂ - 83°C cantilever - 83°C	N ₂ - 83°C cantilever: 21°C	N ₂ - 21°C cantilever - 83°C	
Δf_{max} (Hz)	-10.0	-121.909	-0.015	-121.894	Re >> 1
		-121.909	-0.015	-121.894	Re << 1
$FWHM(83^\circ\text{C})/$ $FWHM(21^\circ\text{C})$	1.436	1.189	1.190	0.999	Re >> 1
		1.170	1.170	1.000	Re << 1
$A_{max}(83^\circ\text{C})/$ $A_{max}(21^\circ\text{C})$	0.408	0.843	0.840	1.003	Re >> 1
		0.856	0.855	1.002	Re << 1

but are real aspects of the gas condition to be included in the analyte data signature. These observations on the peak shape change can also be separately expressed in terms of the ratios (83°C to 21°C) of A , and of $FWHM$ (Table 2); clearly, peak attenuation and broadening is only significant in Scenarios 2 and 3, where the gas properties dominate the behavior. In contrast, the peak frequency shifts Δf_{max} (Table 2, top) are most significant in Scenario 3 where the resonator is hot, indicating that thermal effects on the modulus dominate over gas damping for this type of resonance change. The large Δf_{max} value of -122 Hz is based on a modeled +62°C temperature change for the resonator, whereas the measured frequency shift under the same presumed ΔT is a much more modest -10 Hz (Fig. 2). If we assume that the true resonator temperature is significantly less than the measured 83°C, we can then set the theoretical $\Delta f_{max} = -10$ Hz to back out the corresponding temperature increase. In the context of Scenario 3, this yields a much smaller $\Delta T = +5^\circ\text{C}$ (21°C → 26°C). Such a discrepancy between the actual and measured temperature changes experienced by the resonator is consistent with the somewhat remote placement of the thermocouple probe, as described previously. Also, the COTS resonator design, with the silicon cantilever mounted onto a plastic chip for handling and electrical connectivity purposes, is in somewhat poor thermal contact with the heated body of the gas cell, lending further credence to the notion of a relatively cool resonator. The general agreement of both the Q -factor change and frequency shift (with corrected ΔT above) predicted in Scenario 2 with the corresponding measured values, in conjunction with the thermal radiation calculation using Eq. 2, appear to support an interpretation of the experimental setup as one with a heated gas and a comparatively cool resonator. More importantly, the fundamental mode calculations **identify peak frequency shift as the resonance change most affected by the thermally-induced, internal changes to the resonator modulus – that is, by thermal drift**. If these conclusions regarding the peak shape change and frequency shift also hold for the overtone mode, then the elegant strategy of thermal drift self-compensation demonstrated by Naeli and Brand should also be applicable in the cfDRD method, where the preliminary measurements of the TCF (presented at the beginning of this section) indicate a close similarity in value between the fundamental and overtone resonances. The non-identical changes in Q -factor observed for these two resonance modes (Figs. 2 and 3, respectively) do not derive from changes in the intrinsic properties of the resonator. Therefore, such changes do not represent thermal drift and will correctly be retained, rather than mutually cancelled, upon assessing a differential response between the two resonances. The calculations also provide potential insight into the observed, negligible Q -factor decrement for the overtone with increased temperature (Fig. 3). If gas damping is principally

responsible for changes in the Q -factor, then any mode which is insensitive to this external phenomenon should suffer no peak shape changes upon heating or cooling. We have previously found that the overtone at ~ 399 kHz is apparently unresponsive to compositional changes in the surrounding gas,¹ providing more circumstantial evidence to support the foregoing analysis.

To improve upon the data shown in Figs. 2 and 3, we have transitioned from the two sets of benchtop instrumentation described above to a single test platform based on a lock-in amplifier with a compact form factor (PCI bus expansion card). This low-noise amplifier (Anfatec AMU 2.4)¹⁶ has a frequency range of 3 mHz to 2 MHz, and a reference output of 0.3 mV to 10 V, permitting excitation and read-out of both the fundamental and 4th resonance modes using a single device. At the maximum frequency range, a resolution of less than 1 Hz can be achieved. This improvement will allow a much more accurate acquisition of the resonance spectra and assessment of peak frequency shift and shape change.

1.3 Resonance Peak Fitting Algorithm

In our previous and current reports, we presented/present data as high-frequency-resolution spectra; changes in the included resonance peaks, due to changes in the gas composition and temperature, were assessed by generating consecutive series of spectra and performing an analysis of these data *ex post facto*. As was noted (Section 1.3.1 of Ref. 1), the simultaneous requirements of rapid data acquisition and high frequency resolution leads to data-, processor-, and time-intensive demands on the sensor system. One strategy proposed to help alleviate these burdens is the usage of functions which could be fit with high fidelity to lower resolution spectral data. Prior attempts to use Gaussian and Lorentzian functions (and variations thereof) failed to adequately model the peak shapes.¹ The coupling of electrical and mechanical behaviors in the piezoelectric resonator drive element creates the resonance/anti-resonance phenomenon responsible for the asymmetric peak shape; the relative prominence of this asymmetry can be somewhat tuned by the circuit design, since the resonances in the test setup are currently measured indirectly with an AC bridge circuit.¹

An algorithm was developed in FY12 to produce high quality fits to the resonance peaks. The details of this algorithm are provided in Appendix C, and involve the use of a hybrid function based on a fit developed by Doniach and Šunjić for X-ray photoelectron spectroscopy (XPS) spectral lines.¹⁷ As is frequently done in the analysis of XPS data, separate fits are applied to the resonance peak above and below the peak frequency value f_{max} ; in the present case, the same functional form is used in both frequency domains. Once f_{max} and the corresponding resonator response value y_{max} (where y_{max} minus the local baseline value defines the response amplitude A) are defined, the fitting function relies on only four adjustable parameters, two for each frequency domain of the hybrid fit: 1) a peak width parameter γ ; 2) an asymmetry parameter α which controls the skewness about f_{max} . To demonstrate this algorithm, fits were applied to several spectra corresponding to the fundamental resonance in pure N₂, an equimolar mixture of N₂ and He, and pure He (Fig. 4). Although these test fits were performed with manual adjustments of γ and α , in practice optimal curve fitting would be performed with a Levenberg-Marquardt or similar standard algorithm.

An obvious drawback of this approach is the need to locate the peak frequency – this must be accomplished without performing a high-resolution frequency sweep, as this would defeat the purpose of the algorithm. One solution is to simply treat f_{max} and y_{max} as fifth and sixth

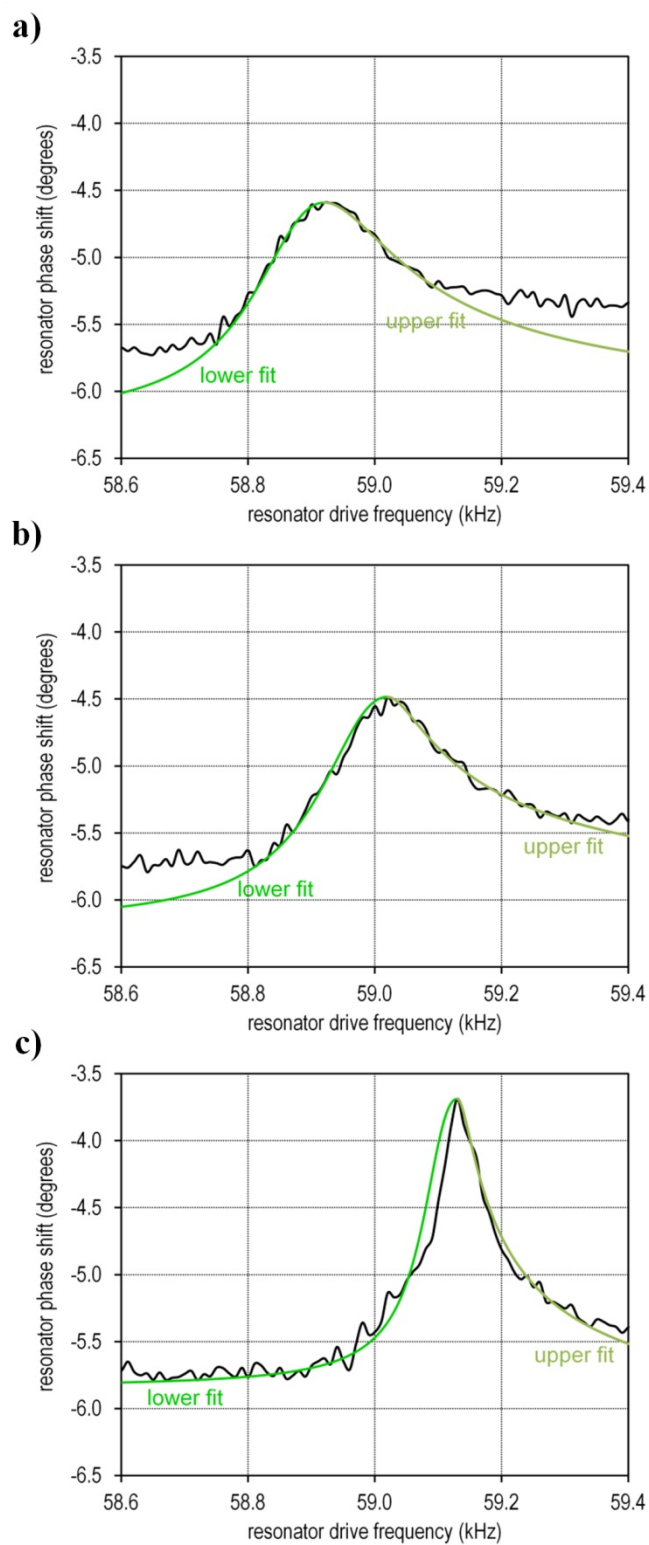


Figure 4. Frequency spectra for the fundamental resonance mode of a Bruker Active Probe cantilever in: a) pure N_2 , b) an equimolar mixture of N_2 and He, and c) pure He at $21^\circ C$. Hybrid functional fits, as described in Appendix C, are superimposed on each plot.

adjustable parameters. The full frequency span of a resonance mode for a given resonator can be practically defined by its behavior in the most dense/viscous and least dense/viscous pure gases which may possibly be detected in the sensor application; such gases might include tungsten hexafluoride, radon, and xenon in the former limit, and hydrogen and helium in the latter limit. Any admixture of these limiting cases will then produce an intermediate value of f_{max} . A calibration scan with an appropriate gas – say, a gas of moderate density/viscosity like N_2 – through the full frequency span, followed by application of the algorithm, then provides good initial values for the parameters. During subsequent sensor operation, the algorithm may then be applied in near real-time to the pre-determined, sparse set of monitored frequencies.

1.4 (Quartz Crystal Tuning Fork)-Based cfDRD Platform

Although our research and development efforts in FY12 have been focused primarily on confirming the viability of thermal drift compensation for the cfDRD sub-sensor, we have also initiated efforts in the development of a successor system. A breadboard-level prototype was developed which is intended to eventually replace all of the benchtop-scale test instrumentation described in our previous report.¹ This integration of functionality represents the first and most important step down a critical path towards a fully miniaturized, self-contained sensor array system.

The key elements of the first-generation integrated cfDRD solution are: 1) an ECS ECS-.320-12.5-13X 32.768 kHz quartz crystal tuning fork resonator, which serves as the cfDRD sensor transducer; 2) a Microchip Technology PIC24FJ64GB002 low-power microprocessor; 3) an Analog Devices AD9833 programmable waveform generator; 4) two LM324A quad amplifiers; 5) two Analog Devices AD620 instrumentation amplifiers and; 6) an Analog Devices AD630 balanced modulator/demodulator for use as a lock-in amplifier. The ECS-31X series tuning fork has a compact radial lead package (2.1 mm diameter by 6.2 mm length), and a nominal TCF of -0.034 ppm/°C in the -10°C to 60°C operational temperature range. The PIC24FJ64GB002 is the 28-pin dual in-line package (DIP) version of the PIC24FJ64GB004 series microcontroller. This microprocessor includes 64K bytes of programming space, 8K bytes of memory, and nine 10-bit analog-to-digital (A/D) converters; these features provide a large programming space and the ability to digitize several analog points for analysis. The AD9833 waveform generator is capable of producing sine, triangular or square-wave outputs. Its 24-bit programmable frequency register, with a 25 MHz clock rate, has a resolution of 100 mHz; for comparison, at a 1 MHz clock rate a resolution of 4 mHz can be achieved over the 0-12 MHz range. LM324A quad amplifiers have been included in this prototype for tuning purposes, to provide any level shifting and system gain that may be needed as the circuit is optimized. The AD620 instrumentation amplifiers are used to buffer the inputs to the AD630 balanced modulator/demodulator. This device features signal recovery from 100 dB of noise, a 2 MHz channel bandwidth, is pin programmable with closed-loop gains of ± 1 and ± 2 , and has 0.05% closed-loop gain accuracy and match.

1.4.1 Hardware Description

The circuit, as an initial design integrating all of the required functional elements for cfDRD, contains several adjustable features not intended to survive into the final production system, but which allow testing and optimization in the current stage of development. The power

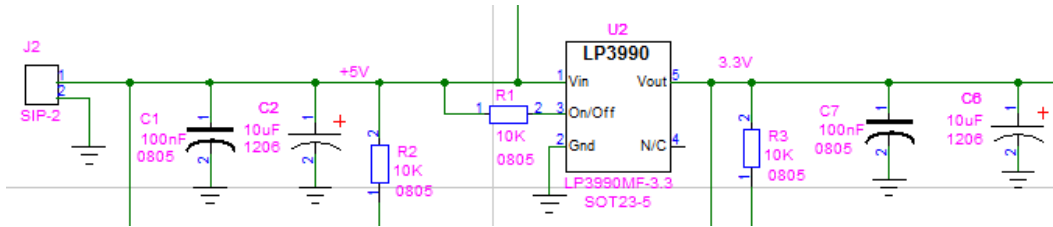


Figure 5. Power circuit for 1st generation integrated cfDRD sensor.

section (Fig. 5) consists of some conditioning and an LP3990 low-dropout regulator (4-6 volt input to 3.3 volt output) which can supply up to 150 mA of current. The PIC24FJ64GB002 microprocessor (Fig. 6) has a wide operating range from 2.0-3.3 V, and chips in the same low-power family are available down to 1.5 V. In this design, we are using the 8 MHz internal oscillator, so no separate crystal is needed. The chip also has a built-in USB interface that, while wired in the current schematic, is not presently planned for usage. Ain1, Ain2, Ain3 and Ain4 are the four analog inputs for the A/D converter. Ain1 receives the output of the AD9833 waveform generator and will be used to monitor the frequency that is being generated, while Ain2 is the output of a level shifter/gain stage that may be required before driving the 32 kHz tuning fork resonator (Fig. 7). Note that the jumper JP5 selects whether the gain stage is utilized or not; in the event that the gain stage is not used, Ain2 and Ain1 become identical. Ain3 is the output of two gain stages and the input to U3, one of the buffer amplifiers for the AD630 modulator (Fig. 8); the two amplifiers are present to provide additional gain if needed. Ain4 is the final output of the AD630 modulator, which functions as a lock-in amplifier, and the low-pass filters (Fig. 9); this output represents the ultimate measurement signal. Finally, another optional gain stage is included after the filters to boost the output signal if necessary. The AD9833 waveform generator (Fig. 10) is intended to provide a highly stable AC drive signal to the tuning fork resonator. U5 is the clock signal for U8 (the AD9833), and is currently a 4 MHz crystal; this oscillator can be replaced with any oscillator having a DIP form factor and frequency range 1-25 MHz. SIP-3 selects the drive voltage for the waveform generator and oscillator, which will both operate at either 3.3 or 5 volts; the former bias will represent typical operations. The output frequency of the AD9833 is given by the equation:

$$(3)$$

where $FreqREG$ is a 28-bit integer value loaded in the register as two 14-bit words, and f_{MCLK} is

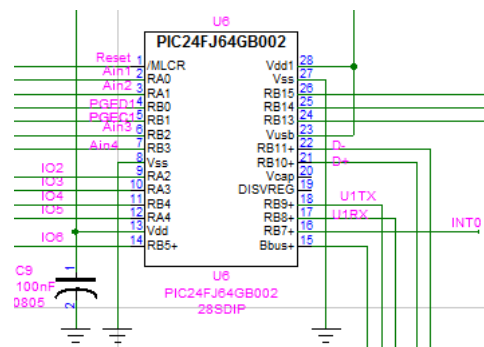


Figure 6. Microprocessor for 1st generation integrated cfDRD sensor.

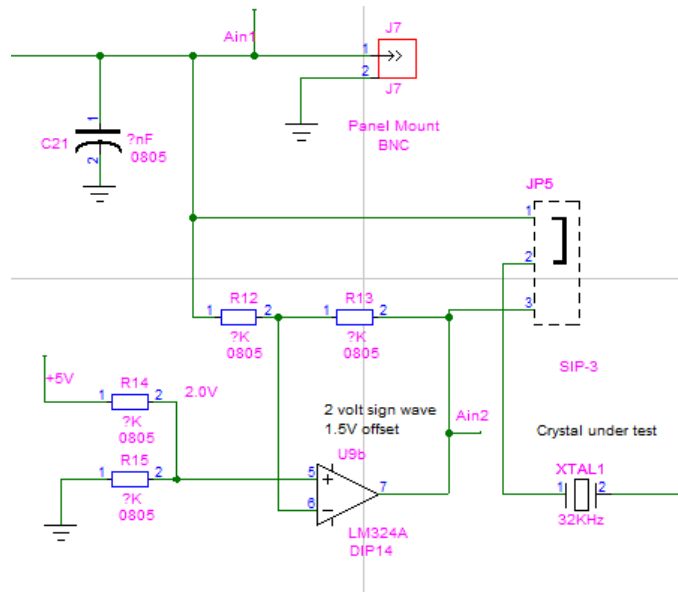


Figure 7. Circuit for 1st generation integrated cfDRD sensor: buffer to quartz-crystal tuning fork.

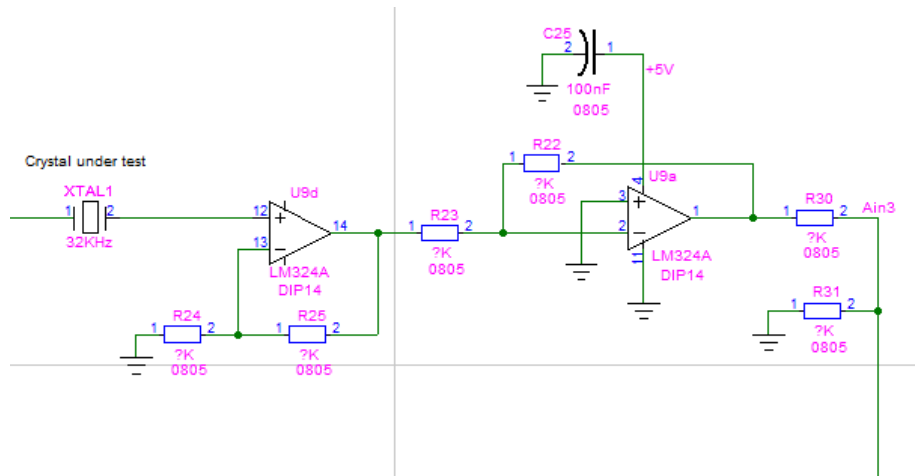


Figure 8. Circuit for 1st generation integrated cfDRD sensor: tuning fork output to lock-in amplifier.

the clock frequency. For coarse tuning of the frequency, only the upper 14-bit value needs to be modified; for finer tuning, the lower 14-bit value must also be changed. In the present case of a 32.768 kHz resonator and $f_{MCLK} = 4$ MHz, the upper register value is $\text{FreqREG} = 488$; this coarse value alone produces an output frequency of 32.749 kHz. The output phase shift of the waveform generator is similarly described by:

$$(4)$$

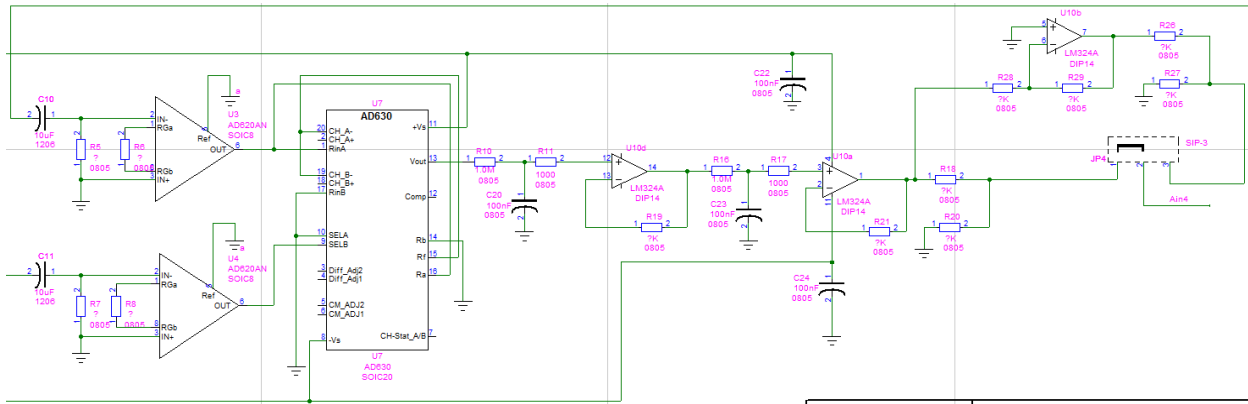


Figure 9. Circuit for 1st generation integrated cfDRD sensor: lock-in amplifier, filters, and final gain stage.

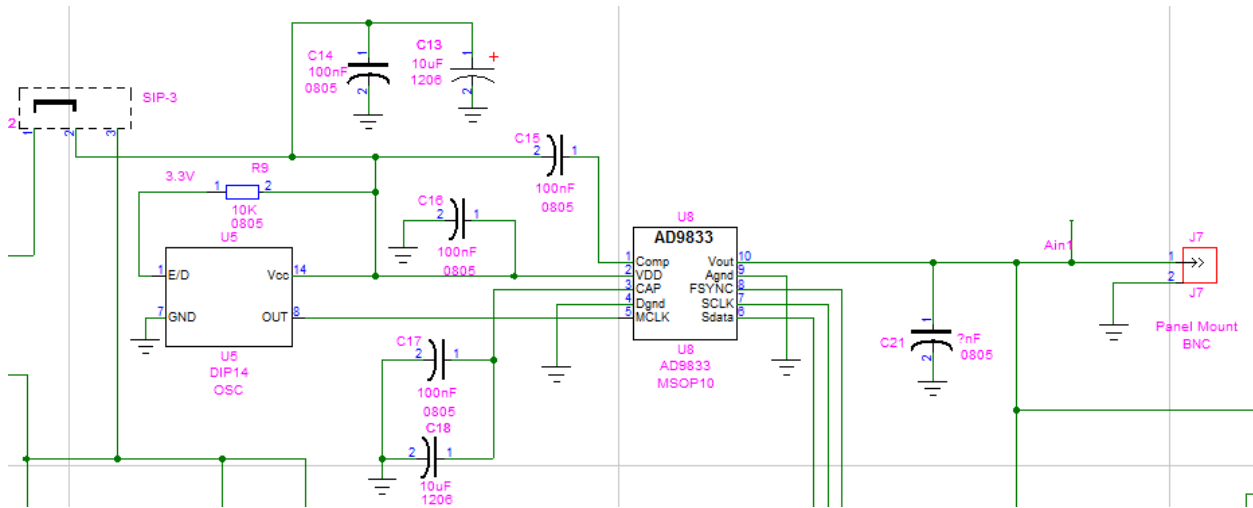


Figure 10. Waveform generator for 1st generation integrated cfDRD sensor.

1.4.2 Software Description

At the conclusion of FY12, the control software was being written in C using a compiler for embedded microprocessor applications (CCS). The PIC24FJ64GB002 chip was being loaded and tested using MPLAB X Integrated Development Environment version 1.3 (Microchip Technology). In addition, a LabVIEW interface will be designed to provide a versatile interface with the C code. Several features are planned, including: 1) a simplified graphical user interface for programming of the waveform generator; 2) sweep recording for the A/D converter to help with function programming and; 3) general diagnostics.

1.5 TCD Sub-Sensor Developmental Path

The readout electronics for the TCD sub-sensor was previously designed for chemical vapor detection using polymer-coated piezoresistive microcantilevers (Cantion CantiChip4 arrays),¹⁸ and adapted without modification to the current application. This modular circuit is comprised of a digital board, which performs data processing and readout through Universal Serial Bus (USB), and one or more analog boards each with four independent, Wheatstone bridge circuits (quarter bridge), and A/D conversion and amplification (Fig. 11, left). A single pair of analog and digital boards consumes approximately 750 mW of power while fully active; however, only about 170 mW are used by the analog circuitry, apportioned between the A/D converter (160 mW) and the four bridge circuits (10 mW). For applications requiring the sensor to be embedded and fully miniaturized, the USB microcontroller can be excluded to help meet restrictive power budgets. The current TCD sub-sensor electronics may be merged with those for the cfDRD sub-sensor, which will likely have some form of the hardware architecture described in Section 1.4, to form a fully-integrated sensor array. A careful selection of low-power, small-outline surface mount components, and layout on double-sided printed circuit boards, should allow such a complete sensor array to be as small or smaller than the circuit shown in Fig. 11.

While the analog circuits were designed to function as strain gauges, measuring chemically-induced changes in transducer piezoresistance, any change in the electrical resistance of a sensing element can be detected sensitively. The large temperature coefficient of resistance of the Cantion CantiChip4 piezoresistive cantilevers (previously estimated at 2860 ppm/K)¹⁹ allows them to also be used as thermistors, thus enabling the TCD method of gas detection. Unfortunately, Cantion cantilevers are specialized research devices with virtually zero market demand; therefore, in parallel to our transitional work on quartz crystal tuning forks, a search for a suitable mass-produced, high-precision, and low-cost TCD alternative was undertaken during

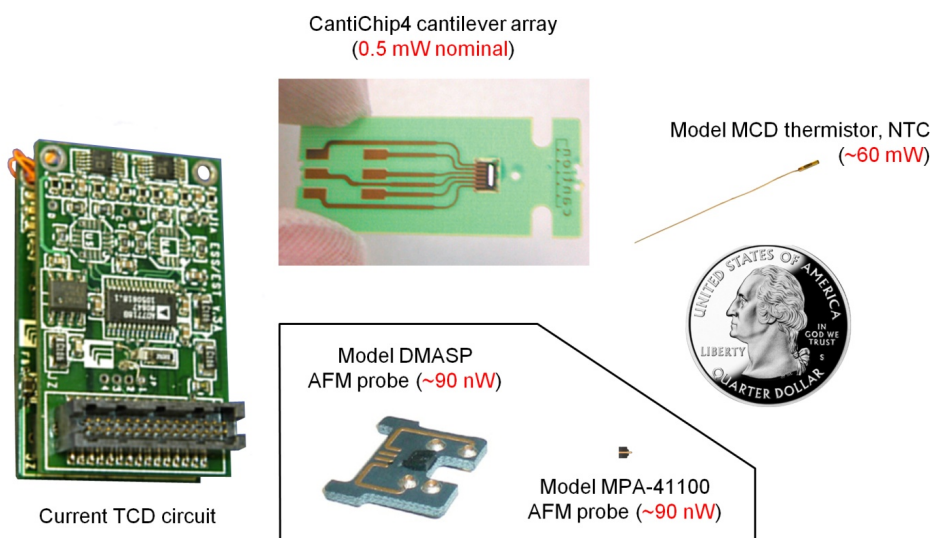


Figure 11. Current electronic circuit for TCD sub-sensor (left), shown with current (Cantion CantiChip4) and mass-produced COTS (Measurement Specialties MCD thermistor) transducers. The current cfDRD transducer (Bruker Active Probe cantilever) is also shown (bottom), in both mounted (wire-bonded) and unmounted versions. All items are shown in correct relative scale, with a U.S. quarter shown for size comparison. The listed power consumption values are estimates based on use in the current TCD circuit, and the cfDRD test circuit described in our previous report.¹

FY12. These efforts uncovered an initially promising candidate: a negative temperature coefficient (NTC) miniature thermistor (Measurement Specialties MCD probe). However, while the manufacturer did not list the power threshold for self-heating, documentation for a similar device (EPCOS S869 Series NTC thermistor) indicated a value of approximately 60 mW, which may be prohibitively high for the most demanding embedded applications; therefore, custom fabricated transducers are probably required in such cases.

1.6 Conclusion

In Fiscal Year 2012, we have constructed an experimental apparatus for testing the viability of thermal drift compensation in the cfDRD method of gas detection. The data obtained from this test setup reveals similar TCF values for the fundamental and 4th overtone resonance modes obtained upon heating from 21°C to 83°C, in agreement with the previous results reported by Naeli and Brand; however, a significant decrement in Q -factor for the same temperature change was observed for the former mode, but not the latter. Using simple theoretical models, the downshifts in resonance peak frequency – as represented by the TCF – can be attributed to a softening of the cantilever material modulus with increased temperature, while the peak amplitude attenuation and broadening under the same conditions is due almost entirely to alterations in the density and viscosity of the gaseous medium. We therefore tentatively conclude that the cfDRD thermal drift, by definition an intrinsic property of the resonator, is exhibited only in the peak frequency shift (TCF) and not in the peak shape change (Q -factor). We have also developed an algorithm for fitting hybrid functional curves to resonance spectra in the frequency domain, and have successfully applied this method to a series of data with changing gas composition. Early efforts towards developing a cfDRD successor system were initiated in FY12, and a new circuit was designed around a mass-produced, high-precision, and low-cost quartz crystal tuning fork.

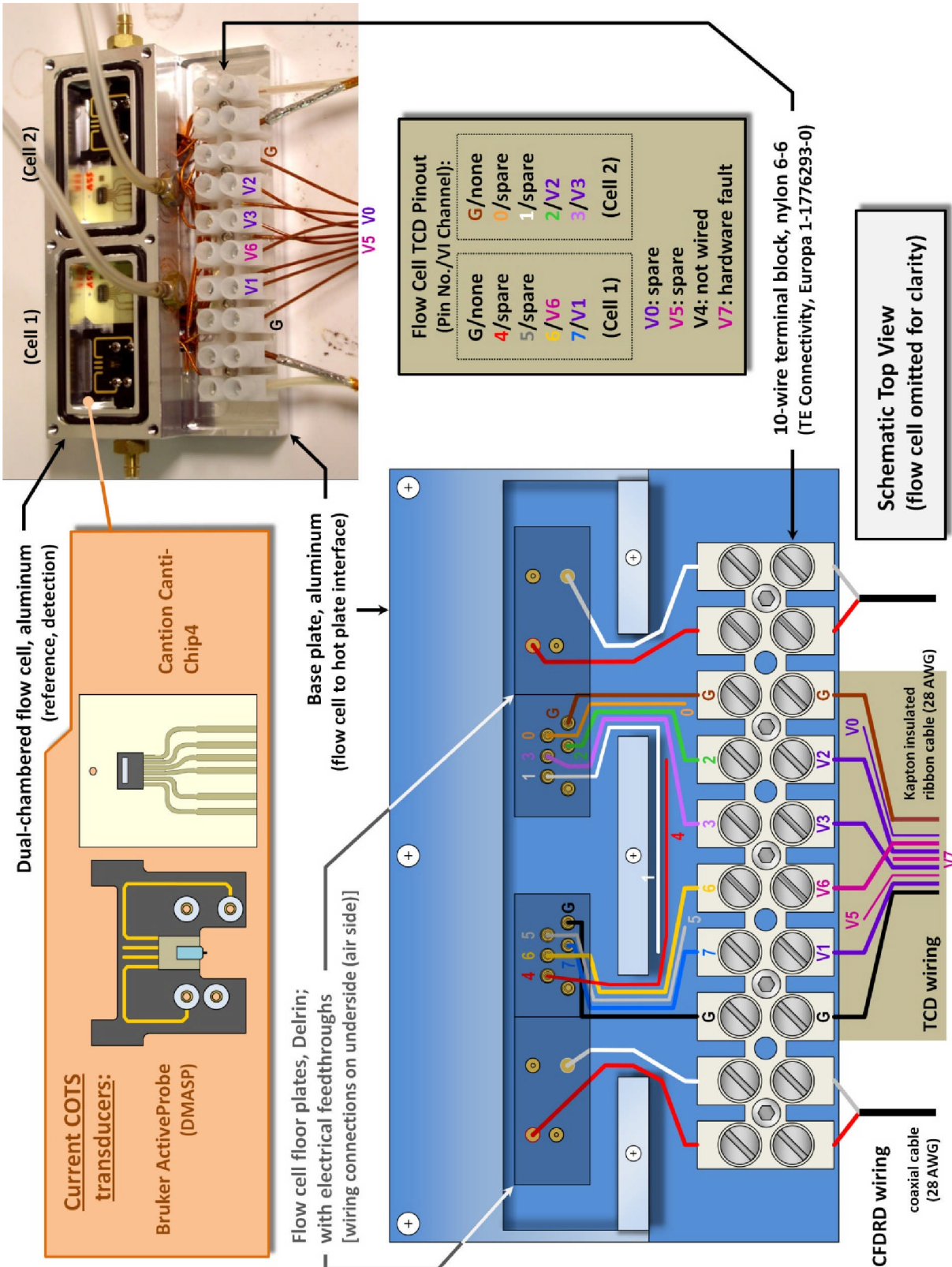
This work was performed under the auspices of the U.S. Department of Energy by Lawrence Livermore National Laboratory under Contract DE-AC52-07NA27344.

1.7 References

- ¹ A. Loui and S. K. McCall, LLNL Report No. LLNL-TR-509016, 2011.
- ² K. Naeli and O. Brand, *Rev. Sci. Instrum.* **80**, 8 (2009).
- ³ Bruker AFM Probes: <http://www.brukerafmprobes.com>.
- ⁴ Digi-Key Corporation: <http://www.digikey.com>.
- ⁵ G. L. Flowers, B. D. Faubion, J. L. Montague, and S. T. Switzer, Pantex Plant Report No. MHSMP-80-63, 1980.
- ⁶ Loctite Adhesives (Henkel Corporation): <http://henkelna.com>.
- ⁷ A. Loui, D. J. Sirbuly, S. Elhadj, S. K. McCall, B. R. Hart, and T. V. Ratto, *Sens. Actuators A* **159**, 58 (2010).
- ⁸ F. R. Blom, S. Bouwstra, M. Elwenspoek, and J. H. J. Fluitman, *J. Vac. Sci. Technol. B* **10**, 19 (1992).
- ⁹ S. Tétin, B. Caillard, F. Ménil, H. Debéda, C. Lucat, C. Pellet, and I. Dufour, *Sens. Actuator B-Chem.* **143**, 555 (2010).
- ¹⁰ P. Sanz, J. Hernando, J. Vazquez, and J. L. Sanchez-Rojas, *J. Micromech. Microeng.* **17**, 931 (2007).
- ¹¹ G. Y. Chen, R. J. Warmack, T. Thundat, D. P. Allison, and A. Huang, *Rev. Sci. Instrum.* **65**, 2532 (1994).
- ¹² D. R. Lide ed., *CRC Handbook of Chemistry and Physics* (CRC Press, Boca Raton, FL, 2005).
- ¹³ NIST Chemistry WebBook: <http://webbook.nist.gov/chemistry/>.
- ¹⁴ J. E. Hatch ed., *Aluminum: Properties and Physical Metallurgy* (ASM International, Materials Park, 1984).
- ¹⁵ B. Leckner, *Combust. Flame* **19**, 33 (1972).
- ¹⁶ Anfatec Instruments AG: <http://www.anfatec.de>.
- ¹⁷ S. Doniach and M. Šunjić, *J. Phys. C: Solid State Phys.* **3**, 285.
- ¹⁸ A. Loui, T. V. Ratto, T. S. Wilson, S. K. McCall, E. V. Mukerjee, and B. R. Hart, *Analyst* **133**, 608 (2008).
- ¹⁹ A. Loui, S. Elhadj, D. J. Sirbuly, S. K. McCall, B. R. Hart, and T. V. Ratto, *J. Appl. Phys.* **107**, 054508 (2010).
- ²⁰ S. N. Mahmoodi, N. Jalili, and M. Ahmadian, *Nonlinear Dyn.* **59**, 397 (2010).
- ²¹ F. M. White, *Fluid Mechanics* (McGraw-Hill, New York, 1999).
- ²² Y. C. Fung, *An Introduction to the Theory of Aeroelasticity* (Dover Publications, New York, 2002).

- ²³ F. Lochon, I. Dufour, and D. Rebière, *Sens. Actuators B* **118**, 292 (2006).
- ²⁴ X. X. Li, T. Ono, Y. L. Wang, and M. Esashi, *Appl. Phys. Lett.* **83**, 3081 (2003).
- ²⁵ R. Lifshitz and M. L. Roukes, *Phys. Rev. B* **61**, 5600 (2000).
- ²⁶ A. A. Geisberger, N. Sarkar, M. Ellis, and G. D. Skidmore, *J. Microelectromech. Syst.* **12**, 513 (2003).
- ²⁷ H. J. M. Hanley, R. D. McCarty, and W. M. Haynes, *J. Phys. Chem. Ref. Data* **3**, 979 (1974).
- ²⁸ U. K. Deiters, *AIChE J.* **48**, 882 (2002).
- ²⁹ J. Jeong, S. Chung, S. Lee, and D. Kwon, *J. Microelectromech. Sys.* **12**, 524 (2003).

Appendix A: Gas Cell Wiring Diagram



Appendix B: Analysis of Thermally-Induced Changes in the Fundamental Resonance of a Microcantilever

Microcantilevers undergoing flexural oscillation in a fluid medium may be modeled using the classical, one-dimensional (1-D), driven, damped oscillator equation provided that: 1) the oscillatory amplitude A is much less than the cantilever thickness h (weak-axis bending is presumed); 2) the cantilever length L is much greater than its width b and, most importantly, its thickness; 3) the fluid may be treated as an isotropic continuum; 4) the fluid is incompressible and; 5) the damping, relative to oscillation in a vacuum, is due entirely to viscous (i.e., viscosity related) or inertial (i.e., density related) effects.

These conditions are largely met in the present case with the COTS resonator (Bruker Active Probe) immersed in a gaseous medium. For the fundamental resonance of the cantilever, $A \cong 10$ nm for an applied bias of $0.5 V_{\text{rms}}$,¹⁰ while h is nominally $4 \mu\text{m}$.³ The cantilever thickness is 1% of L ($4 \mu\text{m}$ vs. $375 \mu\text{m}$), but the dual-width design has a basal width of 67% ($250 \mu\text{m}$ vs. $375 \mu\text{m}$) and distal width of 15% ($55 \mu\text{m}$ vs. $375 \mu\text{m}$) of the total length.^{3, 20} The Knudsen number Kn ,²¹ defined as the ratio of the gas mean free path λ to the characteristic length l (interpreted as L), can be calculated at room temperature and 1 atm:

$$Kn = \frac{\lambda}{l} = \frac{\frac{k_B T}{4\sqrt{2}\pi r_w^2 P}}{l} = \frac{k_B T}{4\sqrt{2}\pi r_w^2 P l} = \frac{(1.3806 \times 10^{-23} \text{ J/K})(293 \text{ K})}{4\sqrt{2}\pi(2.25 \text{ \AA})^2(101325 \text{ Pa})(375 \mu\text{m})} = \frac{4.44 \times 10^{-2} \mu\text{m}}{375 \mu\text{m}} = 1.18 \times 10^{-4} \quad (\text{B1})$$

where the van der Waals radius r_w for N_2 was used; evidently, the gas ‘appears’ to the cantilever as a continuous medium. Relative compression and rarefaction effects on the gas due to the cantilever oscillation can be neglected if the Strouhal (St) and Mach (Ma) numbers are both much less than one.²² Letting the characteristic length equal A (~ 10 nm), and assuming a linear gas flow rate $v = 0.35$ cm/s (i.e., the volumetric flow rate 30 sccm times the 1.42 cm^2 cross sectional area of the gas cell chamber),¹ the two parameters for an Active Probe cantilever oscillating at its fundamental resonance (frequency $f_1 \cong 57.4$ kHz) in N_2 at room temperature are calculated as²¹

$$St = \frac{f_1 l}{v} = \frac{(57.4 \text{ kHz})(10 \text{ nm})}{0.35 \text{ cm/s}} = 0.16 \quad (\text{B2})$$

$$Ma = \frac{v}{c} = \frac{v}{\sqrt{\frac{\gamma RT}{M}}} = \frac{0.35 \text{ cm/s}}{\sqrt{\frac{(1.400)(8.3145 \text{ J/mol}\cdot\text{K})(293 \text{ K})}{2.801 \times 10^{-2} \text{ kg/mol}}}} = \frac{3.50 \times 10^{-3} \text{ m/s}}{349 \text{ m/s}} = 1.00 \times 10^{-5} \quad (\text{B3})$$

These values imply that the fluid is relatively incompressible under the representative conditions of resonant operation.

Finally, for a cantilever with the relative dimensions and aspect ratio (length to lateral dimension) of the Active Probe, damping other than viscous and inertial effects should be comparatively negligible according to the analysis by Lochon and co-workers.²³ These other damping effects include: 1) mechanical dissipation into the support substrate; 2) acoustic radiation into the gas and; 3) thermoelastic heating loss within the cantilever. The bulk and rigidity of the support relative to the cantilever disallows significant work done on the former by oscillations of the latter; the Q -factor corresponding to support loss is proportional to $(L/h)^3$ – here: $(375 \mu\text{m}/4 \mu\text{m})^3 = 8 \times 10^5$ – such that this dissipation effect becomes significant only when the aspect ratio is reduced towards unity.²³ We showed above (Eqs. B2 and B3) that density fluctuations created by the cantilever oscillation are not significant in the present case, implying

that the energy dissipated by acoustic wave generation in the gas is negligible compared to the input excitation energy. The argument for ignoring acoustic radiation losses can be further shown by determining whether $\lambda_o/\lambda_a < 1$, where λ_o is the oscillation wavelength – essentially the displacement wavelength along the cantilever – and λ_a is the acoustic wavelength in the gas. For the fundamental mode of the Active Probe, the oscillation wavelength is estimated as²³

$$\lambda_o = \frac{L}{L\sqrt{4\pi f_1 \left(\frac{3\rho_c}{E_c h^2}\right)^{\frac{1}{4}}}} = \frac{1}{\sqrt{4\pi f_1}} \left(\frac{E_c h^2}{3\rho_c}\right)^{\frac{1}{4}} = \frac{1}{\sqrt{4\pi(57.4 \text{ kHz})}} \left[\frac{(130 \text{ GPa})(4 \mu\text{m})^2}{3(2329 \text{ kg/m}^3)}\right]^{\frac{1}{4}} = 155 \mu\text{m} \quad (\text{B4})$$

where the Young's modulus E_c and density ρ_c for the cantilever are represented by the corresponding values for silicon.^{12, 24} The acoustic wavelength generated by the oscillator in the fundamental mode is obtained simply by dividing the speed of sound c by f_1 which, for N₂ at room temperature, is (349 m/s)/(57.4 kHz) = 6080 μm. Therefore, the neglect of acoustic radiation losses is justified. Thermoelastic damping arises from thermal agitation of the cantilever material from oscillation; Lifshitz and Roukes expressed the Q -factor dependence of this phenomenon on a quantity ξ defined as

$$\xi = h \sqrt{\frac{\pi f \rho_c C_c}{k_c}} \quad (\text{B5})$$

where C_c and k_c are the specific heat capacity and thermal conductivity of the cantilever (respectively), and Q is minimized when ξ equal approximately 2.22.²⁵ Substituting $f = f_1$, and again representing the cantilever properties with those of silicon ($C_c \cong 730 \text{ J/kg}\cdot\text{K}$, $k_c \cong 145 \text{ W/m}\cdot\text{K}$ at 300 K),²⁶ we find that $\xi = 0.18$, placing the operating conditions well away from those where internal heating loss is expected.

With these validating assumptions established, we now turn our attention to the analytic solution of the classical, 1-D, driven, damped oscillator equation. The linear differential equation describes the cantilever tip displacement $y(t)$ under the influence of a sinusoidal excitation source, and a viscous drag force proportional to the tip speed:¹¹

$$\begin{aligned} &(\text{inertial force}) + (\text{viscous drag force}) + (\text{cantilever restoring force}) = \text{net force} \\ &m^* \ddot{y} + m^* \gamma \dot{y} + m^* \omega_0^2 y = F_0 e^{i\omega t} \end{aligned} \quad (\text{B6})$$

where the effective cantilever mass m^* is proportional to the cantilever mass m_c , γ is the dissipation constant (i.e., reciprocal time or rate for 1/e dissipation of input excitation energy), F_0 is the total force magnitude, and ω is the angular resonance frequency. The fundamental angular resonance frequency ω_0 of the cantilever in a vacuum is defined in terms of the cantilever spring constant K and m^* :

$$\omega_0 = \sqrt{\frac{K}{m^*}} \quad (\text{B7})$$

The resonance quality factor Q is defined in terms of the ratio of input excitation energy to the energy dissipated by damping over one cycle of oscillation; equivalently, this is expressed as the ratio of the undamped oscillation rate (frequency f_0) to the rate of energy dissipation (γ):

$$Q = 2\pi \frac{f_0}{\gamma} = \frac{\omega_0}{\gamma} \quad (\text{B8})$$

where the definition of angular frequency is used. As the resonator *in vacuo* experiences increased damping (beyond those of internal, mechanical origin) with the advent of gases and liquids, the increase in γ leads to a corresponding drop in the quality factor; this behavior is well-known in atomic force microscopy, where resonant scanning modes are often utilized in aqueous media. The angular frequency ω_{max} in the gas-damped resonance condition is simply related to the vacuum angular frequency and the dissipation constant:

$$\omega_{max}^2 = \omega_0^2 - \frac{\gamma^2}{2} = \omega_0^2 \left(1 - \frac{1}{2Q^2}\right) \quad (\text{B9})$$

where the last equality is trivially derived from Eq. B8. The tip displacement amplitude A is a function of ω , with a maximum value attained at resonance ($\omega = \omega_0$ in a vacuum, $\omega = \omega_{max}$ otherwise) given by:

$$A_{max} = \frac{F_0 Q}{K \sqrt{1 - \frac{1}{4Q^2}}} \quad (\text{B10})$$

Note the typographical error (F_0 vs. f_0) in Eq. 2 (Section 1.3.2) of our previous report.¹ The full width at half maximum (*FWHM*) for the resonance peak in the frequency domain is approximately equal to:

$$FWHM = \frac{\gamma\sqrt{3}}{2\pi} \quad (\text{B11})$$

For weakly-damped systems, as in the present case of gaseous damping, the Q -factor can be expressed in terms of the characteristic peak width:

$$Q = \sqrt{3} \left(\frac{\omega_{max}}{FWHM} \right) \quad (\text{B12})$$

The dissipation constant γ , which determines the degree of damping and the resulting Q -factor (Eq. B8), is a function of the gas density ρ and viscosity η . The resonance amplitude A_{max} also depends on the spring constant K . These properties, both external (ρ , η) and internal (K) to the resonator, are in turn functions of the temperature T ; therefore, alterations in the fundamental resonance condition upon changes in temperature may be predicted using Eqs. B7-B12. An examination of resonance spectra in the frequency domain reveals several types of changes that can be readily described. For temperatures T_1 and T_2 ($T_1 \neq T_2$), these include: 1) peak frequency shift: $\Delta f_{max} = f_{max}(T_2) - f_{max}(T_1)$; 2) peak amplitude ratio: $A_{max}(T_2)/A_{max}(T_1)$; 3) Q -factor ratio: $Q(T_2)/Q(T_1)$.

For completeness, we consider the calculation of these three thermally affected quantities in both the inertial and viscous damping regimes, for which the Reynolds number Re is by definition much greater and much less than unity (respectively).²¹ **In both regimes, the cantilever will be modeled as an oscillating sphere of radius R to render the damping expressions tractable.** In the inertial regime, the continuous displacement of gas by the oscillating cantilever gives rise to another damping effect in addition to viscous drag; this effect is due to the substantial inertial mass of the gas relative to the cantilever (hence, ‘inertial’). In this case ($Re \gg 1$), the dissipation constant will be a function of both ρ and viscosity η :¹¹

$$\gamma = \frac{3\pi R^2 \sqrt{2\rho\eta\omega_{max}}}{m^* + \frac{2}{3}\pi\rho R^3} \quad (\text{B13})$$

where the effective mass of the displaced gas is equal to that contained in half of an equivalent sphere of radius R . Substitution of Eq. B13 into Eq. B9 yields the following expression for the gas-damped resonance angular frequency:

$$\omega_{max} = \frac{1}{8} \left(\sqrt{9B^4 + 64\omega_0^2} - 3B^2 \right) \quad (\text{B14})$$

where the quantity B is given by:

$$B = n_1 \left[\frac{(3\pi R^2)(2\rho\eta)}{m^* + \frac{2}{3}\pi\rho R^3} \right] \quad (\text{B15})$$

The coefficient n_1 is a form factor introduced to adapt the calculation, based on a model spherical geometry, to the actual rectangular geometry of the cantilever. The parameters R and n_1 should be constants specific to the cantilever and independent of the gaseous medium; therefore, we can obtain them empirically by using representative measured values for the quantities in Eqs. B13-B15. For the resonance in N_2 at $T_1 = 21^\circ\text{C}$ (Fig. 2, Section 1.2.1), we find that $f_{max}(21^\circ\text{C}) = 57,355.0 \text{ Hz}$ [$\omega_{max}(21^\circ\text{C}) = 360,372.1 \text{ Hz}$] and estimate the $FWHM(21^\circ\text{C})$ at 165.0 Hz , yielding $Q(21^\circ\text{C}) = 602.1$ (Eq. B12). The vacuum angular frequency is then obtained using Eq. B9, and the value $\omega_0(21^\circ\text{C}) = 360,372.3 \text{ Hz}$ plugged into Eq. B8 to give a dissipation constant $\gamma(21^\circ\text{C}) = 598.6 \text{ Hz}$. Using a nominal cantilever spring constant $K(21^\circ\text{C}) = 3 \text{ N/m}$,³ Eq. B7 yields an effective mass $m^* = 2.3 \times 10^{-11} \text{ kg}$. The N_2 density is calculated from the ideal gas law as $\rho(21^\circ\text{C}) = 1.16 \times 10^{-3} \text{ g/cm}^3$, using the molar mass $M = 28.01348$,¹² while the viscosity $\eta(21^\circ\text{C}) = 1.76 \times 10^{-5} \text{ Pa}\cdot\text{s}$ is obtained from a fit to data reported by Hanley and co-workers.²⁷ Equation B13 can be expressed as a cubic equation in R :

$$\left(\frac{2}{3}\pi\rho\gamma \right) R^3 + \left(-3\pi\sqrt{2\rho\eta\omega_{max}} \right) R^2 + \gamma m^* = 0 \quad (\text{B16})$$

which can be solved using Cardano's method.²⁸ An artificially large simple root $R = 24.9 \text{ mm}$ results which, when substituted into the combination of Eqs. B14 and B15, gives a value $n_1 = 1.28 \times 10^2$. The cubic equation also yields a double root $R = 69.2 \text{ nm}$ which is more consistent with the size scale of the cantilever but, upon completion of the calculation (as described below), an unphysical Q -factor prediction is obtained that is five orders of magnitude too large; we thus reject the smaller model sphere radius value.

Armed with the parameters R and n_1 , we may now predict changes to the resonance condition caused by relative heating or cooling. We will assume, in the following calculations, that both the resonator and its gaseous environment are at the same temperature; however, non-equal temperatures may be easily applied as dictated by the appropriate sensor application scenario, although steady-state conditions will always be presumed. For simplicity, we treat the cantilever as monolithic silicon and use the empirical temperature dependence derived by Jeong and co-workers for the Young's modulus (Pa):²⁹

$$E_{Si}(T) = 167.98 \times 10^9 - 1.167 \times 10^7 T + 1757.9 T^2 \quad (\text{B17})$$

with T specified in degrees Celsius. The temperature-dependent spring constant may then be expressed as:

$$K(T) = n_2 \left[\frac{E_{Si}(T)h^3b}{4L^3} \right] = \left(\frac{n_2 h^3 b}{4L^3} \right) E_{Si}(T) = G \cdot E_{Si}(T) \quad (\text{B18})$$

where n_2 is another form factor, and all of the dimensional constants are consolidated into a single coefficient G for convenience. We note that the effects of thermal expansion/contraction

of the cantilever are not accounted in the present calculations (see, for example, Ref. 19 for further details). Using Eq. B17 to get $E_{st}(21^\circ\text{C}) = 1.68 \times 10^2$ GPa, and the nominal value $K(21^\circ\text{C}) = 3$ N/m, we obtain $G = 1.79 \times 10^{-11}$ m from Eq. B18. Using the fundamental resonance in N_2 at $T_2 = 83^\circ\text{C}$ (Fig. 3, Section 1.2.1) as an example of relative heating, the vacuum angular frequency is calculated from Eq. B7 using $K(83^\circ\text{C}) = 2.987$ N/m (Eqs. B17 and B18), yielding a value of $\omega_0(83^\circ\text{C}) = 359,606.5$ Hz reduced relative to that prevailing at 21°C . The gas properties at 83°C can be obtained as in the room temperature case, giving a relatively reduced density [$\rho(83^\circ\text{C}) = 9.59 \times 10^{-4}$ g/cm³] and increased viscosity [$\eta(83^\circ\text{C}) = 2.06 \times 10^{-5}$ Pa·s]. Equations B14 and B15 then allow the calculation of the gas-damped resonance angular frequency $\omega_{max}(83^\circ\text{C}) = 359,606.1$ Hz, whereupon the dissipation constant $\gamma(83^\circ\text{C}) = 711.7$ Hz can be calculated from Eq. B13. The Q -factor is then trivially calculated from Eq. B8 as $Q(83^\circ\text{C}) = 505.3$.

Thus, in the inertial regime ($Re \gg 1$), the thermally-induced changes in the fundamental resonance for the exemplary temperature change $+62^\circ\text{C}$ ($21^\circ\text{C} \rightarrow 83^\circ\text{C}$) are computed as follows, beginning with the peak frequency shift: $f_{max}(83^\circ\text{C}) - f_{max}(21^\circ\text{C}) = -121.9$ Hz. The peak amplitude ratio may be obtained from Eq. B10, which takes the simplified form:

$$\frac{A_{max}(T_2)}{A_{max}(T_1)} = \frac{K(T_1)}{K(T_2)} \left[\frac{Q(T_2)}{Q(T_1)} \right]^2 \sqrt{\frac{4[Q(T_1)]^2 - 1}{4[Q(T_2)]^2 - 1}} \quad (\text{B19})$$

Substitution of the values computed above yields $A_{max}(83^\circ\text{C})/A_{max}(21^\circ\text{C}) = 84.3\%$. Finally, the Q -factor ratio is found to be $Q(83^\circ\text{C})/Q(21^\circ\text{C}) = 83.9\%$.

In the viscous regime ($Re \ll 1$), the foregoing calculations become significantly more simple. Under the influence of only viscous drag, the dissipation constant for an oscillating model sphere of radius R is (cf. Eq. B13):¹¹

$$\gamma = \frac{6\pi R \eta}{m^*} \quad (\text{B20})$$

As before, the model radius may be obtained empirically using representative measured values; specifically, by combining Eqs. B20 and B8, and inserting the values $Q(21^\circ\text{C})$ and $\omega_0(21^\circ\text{C})$ obtained previously, we find that $R = 41.6$ μm . The peak frequency shift for the exemplary temperature change $+62^\circ\text{C}$ ($21^\circ\text{C} \rightarrow 83^\circ\text{C}$) can be computed using Eq. B9, requiring: 1) the vacuum angular frequency ω_0 , with temperature dependence through $K(T)$, calculated as before from Eqs. B7, B17, and B18; 2) the dissipation constant γ , with temperature dependence through $\eta(T)$, calculated from Eq. B20. These computations lead to the same numerical result as Eq. B19. The peak amplitude ratio is also obtained from Eq. B19, with the slightly different result $A_{max}(83^\circ\text{C})/A_{max}(21^\circ\text{C}) = 85.6\%$. A minor difference is also found for the Q -factor ratio: $Q(83^\circ\text{C})/Q(21^\circ\text{C}) = 513.5/602.1 = 85.3\%$.

Regardless of whether inertial or viscous effects are dominant for a gas-immersed cantilever undergoing oscillation, the theoretical values calculated above are all consistent with **relatively increased damping of the cantilever oscillation upon increases in temperature from both intrinsic (softening of the cantilever modulus) and extrinsic (gas-based) sources.**

Appendix C: Fitting Algorithm for Asymmetric Resonance Peaks

The asymmetric fitting function proposed Doniach and Šunjić, when adapted to the present case of a resonance spectral peak in the frequency domain, takes the form:¹⁷

$$y_{fit}(f) = \frac{\Gamma(1-\alpha)}{(\gamma^2+f^2)^{\frac{1-\alpha}{2}}} \cos \left[\frac{\pi\alpha}{2} + (1-\alpha)\tan^{-1} \left(\frac{f}{\gamma} \right) \right] \quad (C1)$$

where Γ is the gamma function, α is a dimensionless asymmetry parameter ($0 < \alpha < 1$) which controls the skewness about the frequency $f_{max,fit}$ corresponding to the maximum value of $y_{max,fit}$, and γ is the peak width parameter. The function is approximately centered at $f=0$, with the peak frequency occurring at

$$f_{max,fit} = \gamma \cot \left(\frac{\pi}{2-\alpha} \right) \quad (C2)$$

A plot of Eq. C1 is shown in Fig. C1, with $\alpha = 0.300$ and $\gamma = 0.115$ for illustrative purposes. The asymmetry is self-evident, with output values corresponding to inputs in the range $f < f_{max,fit}$ greater than those in the range $f > f_{max,fit}$.

Figure C2 shows the fundamental resonance peak of a Bruker Active Probe resonator, as measured indirectly in an AC bridge circuit.¹ In order to fit this resonance peak with the generic functional form given in Eq. C1, several modifications must be made: 1) since larger phase shifts occur for frequencies greater than the peak frequency f_{max} , as observed in Fig. C2, the functional trend should be reversed with respect to frequency input; 2) $y_{max,fit}$ should coincide with the maximum phase shift y_{max} . These adaptations to Eq. C1 are simply made by: a) replacing ' f ' with ' $f_{max} - f + f_{max,fit}$ '; b) multiplying by a scaling factor A_1 , with units of $f^{1-\alpha}$ and; c) adding the output offset ($y_{max} - A_1 y_{max,fit}$) to the product of A_1 and Eq. C1. The modified fitting function is then expressed as

$$y_{fit}(f) = \frac{A_1 \Gamma(1-\alpha)}{\left[(\gamma^2 + (f_{max} - f + f_{max,fit})^2) \right]^{\frac{1-\alpha}{2}}} \cos \left[\frac{\pi\alpha}{2} + (1-\alpha)\tan^{-1} \left(\frac{f_{max} - f + f_{max,fit}}{\gamma} \right) \right] + (y_{max} - A_1 y_{max,fit}) \quad (C3)$$

As a simple check, note that when $f = f_{max}$, Eq. C3 yields an output value of y_{max} , as desired.

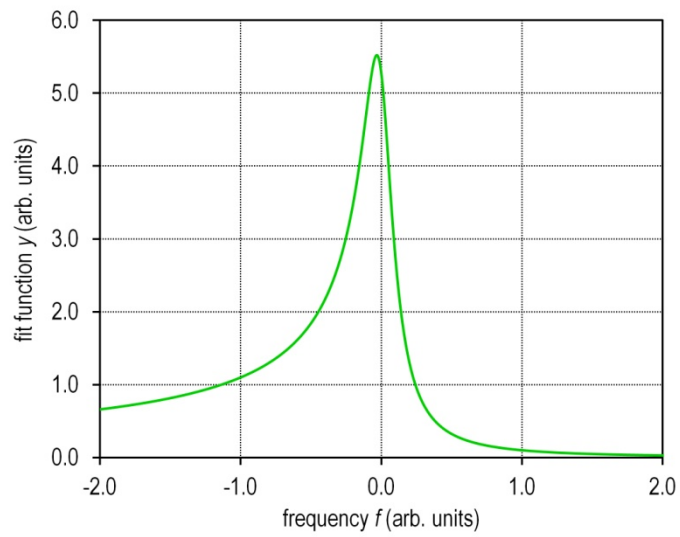


Figure C1. Fitting function (Eq. C1), with $\alpha = 0.300$ and $\gamma = 0.115$.

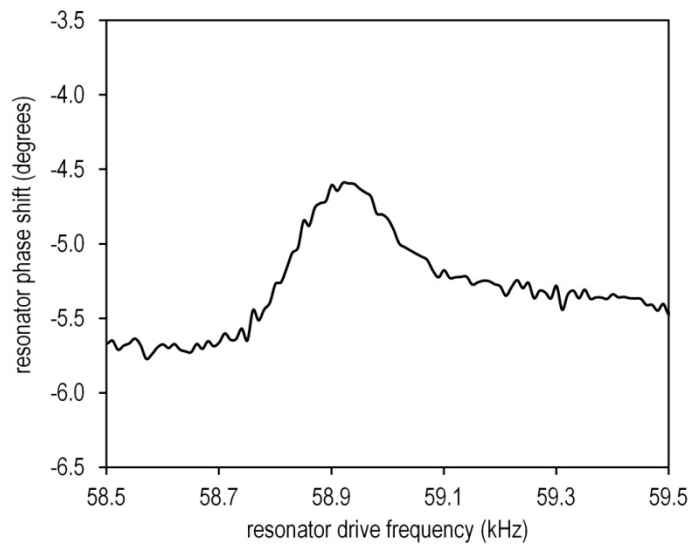


Figure C2. Frequency spectra for the fundamental resonance mode of a Bruker Active Probe cantilever in pure N_2 at 21°C .